DESIGN AND PERFORMANCE ANALYSIS OF AN INTEGRATED GENERATOR–RECTIFIER SYSTEM FOR WIND ENERGY CONVERSION

TEMBA DEEPCHAND[1], PALA SURESH[2]

[1]Student, Department of Electrical and Electronics Engineering, Sanketika Vidya Parishad Engineering College, Visakhapatnam – 530041, Andhra Pradesh, India.

Email: deepchandtemba@gmail.com

[2]Assistant Professor (M.Tech,), Department of Electrical and Electronics Engineering, Sanketika Vidya Parishad Engineering College, Visakhapatnam – 530041, Andhra Pradesh, India.

Email: suresh.eee@svpec.edu.in, Palasuresh369@gmail.com

ABSTRACT

Offshore wind turbines require efficient and reliable power conversion systems. This project proposes an Artificial Neural Network (ANN)-based neuro-adaptive controller for a 10 MW Permanent Magnet Synchronous Generator (PMSG) using an integrated generator–rectifier system for maximum power point tracking (MPPT). The proposed controller replaces conventional PI controllers with ANN-based power and current controllers to improve dynamic response, tracking accuracy, and robustness against parameter variations. The system is evaluated through simulation under different operating conditions, including wind-speed variations, DC-bus voltage sag, and parameter mismatch. The results demonstrate faster response, reduced tracking error, and improved control performance compared with conventional PI control, while maintaining the same MPPT energy yield.

Keywords: Artificial neural network, integrated generator–rectifier, maximum power point tracking, multiport PMSG, offshore wind energy, passive rectifier, power-flow control, Levenberg–Marquardt, adaptive control.

1.INTRODUCTION

1.1 BACKGROUND

The global electricity sector is undergoing a structural transition away from fossil generation towards renewable resources, and wind energy has become one of the principal pillars of this transition. Among wind resources, offshore wind is particularly attractive because sea winds are stronger, steadier and less turbulent than winds over land, and because offshore sites remove most of the visual, acoustic and land-use constraints that limit onshore development. Installed offshore capacity has therefore grown rapidly over the last decade [2]–[5].

To keep the levelized cost of electricity (LCOE) of offshore wind competitive, manufacturers have steadily increased the rating of individual turbines. Commercial platforms now lie in the 10–15 MW class, with rotor diameters well above 160 m [3], [6]–[8], [30]. Larger turbines reduce the number of foundations, cables and maintenance visits per megawatt, but they place severe demands on the electromechanical power conversion chain.

The generator and the power-electronic converter must process many megawatts with very high efficiency, high power density and high reliability, because every hour of downtime at sea is expensive and every kilogram in the nacelle increases tower and foundation cost [9], [13].

1.2 POWER CONVERSION ARCHITECTURES FOR MULTI-MEGAWATT WIND TURBINES

Modern variable-speed wind turbines decouple the rotor speed from the grid frequency through a power-electronic interface. In the dominant "Type 4" (full-converter) arrangement, a permanent magnet synchronous generator

(PMSG) feeds a back-to-back converter that processes the full turbine power [9], [13], [37]. The machine-side converter is usually a two-level pulse-width modulated (PWM) voltage-source converter (VSC) or a three-level neutral-point-clamped (NPC) converter [14]–[16].

At multi-megawatt ratings these conventional architectures face clear obstacles. Each switch of a two-level VSC must withstand the full dc-link voltage and the peak ac current, so devices must be connected in series and/or in parallel, which degrades reliability [13]. NPC converters reduce the voltage stress per device but distribute losses unevenly, which creates thermal hot spots and early failures. Multiport generators feeding several parallel converters reduce the rating of each converter [17]–[19], but every port still requires an active rectifier, so the full turbine power is still processed by switching devices. A comparison of these approaches is sketched in Fig. 1.1.

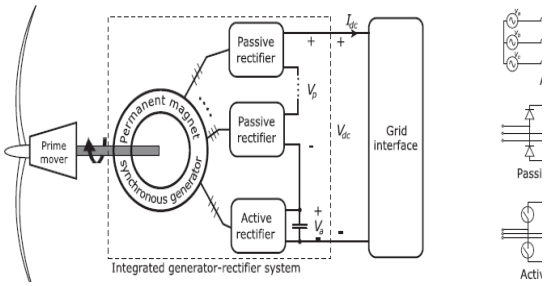


Figure 1.1: Comparison of power-conversion architectures for multi-megawatt PMSG wind turbines

2.LITERATURE REVIEW

2.1 INTRODUCTION

This chapter reviews the literature relevant to the thesis in five areas: generator and converter topologies for large wind turbines, multiport and series-connected dc architectures, maximum power point tracking methods, vector control of PMSG-based rectifiers, and intelligent (ANN, fuzzy and hybrid) controllers in power electronics. The chapter ends with a summary table and a statement of the research gap addressed in this work.

2.2 GENERATOR AND CONVERTER TOPOLOGIES FOR LARGE WIND TURBINES

Polinder *et al.* [37] compared direct-drive and geared generator concepts and showed that direct-drive permanent-magnet generators offer high efficiency and low maintenance, which explains their popularity offshore. Chen, Guerrero and Blaabjerg [12] and Blaabjerg, Liserre and Ma [13] reviewed power electronics for wind turbines and identified the full-scale back-to-back converter as the dominant solution for PMSG turbines, while noting that series/parallel connection of devices at multi-megawatt power reduces reliability. Yaramasu *et al.* [9] surveyed high-power wind energy conversion systems and emphasised the trade-off between switch ratings, switching losses and power density. Wu *et al.* [11] and Wu and Narimani [27] provided comprehensive treatments of high-power converters and drives, including multipulse diode rectifiers with phase-shifting transformers, the concept that underlies the phase-shifted passive rectifiers of the integrated system.

Three-level NPC converters were introduced by Nabae, Takahashi and Akagi [16]. Their neutral-point balancing problem was analysed by Celanovic and Boroyevich [14], and Yazdani and Iravani [15] applied an NPC converter to a direct-drive variable-speed wind unit. These works reduce the voltage stress per device but do not reduce the total power processed by active switches.

2.3 MULTIPORT GENERATORS AND SERIES-CONNECTED DC ARCHITECTURES

Birk and Andresen [17], [18] showed that parallel-connected converters fed by a multiport generator improve efficiency, reliability and

grid harmonics in multi-megawatt turbines. Che *et al.* [19] proposed a six-phase induction generator system with series-connected dc links, demonstrating that series stacking of rectifier outputs can build a higher dc voltage for collection grids. Meyer *et al.* [25] and Robinson, Jovcic and Joos [26] studied dc collection grids for offshore wind farms, which provide the stiff dc interface assumed in this thesis.

Huynh, Wang and Banerjee [20] proposed an integrated PMSG–rectifier architecture for limited-speed-range applications in which most ports feed diode rectifiers and one port feeds an active rectifier. Huynh and Banerjee [21] then introduced active compensation of the dc-voltage ripple produced by the diode rectifiers. Finally, the base paper of this thesis [1] established that the active-rectifier d-axis current controls the total dc-bus power, derived the analytical relation between them, proposed a cascaded PI controller and demonstrated MPPT in simulation and on a three-port laboratory prototype. In that work the PI gains are fixed, and the robustness of the power loop to generator parameter variations is not studied in detail.

3.MODELLING OF THE INTEGRATED GENERATOR–RECTIFIER WIND ENERGY SYSTEM

3.1 SYSTEM DESCRIPTION

The system studied in this thesis is shown in Fig. 3.1. A variable-speed wind turbine shares a common shaft with a multiport PMSG having k = 3 three-phase ac ports. Ports 1 and 2 feed six-pulse diode bridges without output filter capacitors, and port 3 feeds a three-phase two-level IGBT active rectifier with a dc-side capacitor C_a. The dc outputs of the three rectifiers are connected in series and connected to a stiff dc interface of V_{dc} = 5.7 kV. The stiff interface represents either the intermediate dc link of an ac collection system, regulated by a grid-side converter, or a medium-voltage dc collection grid regulated at the substation [1], [25], [26].

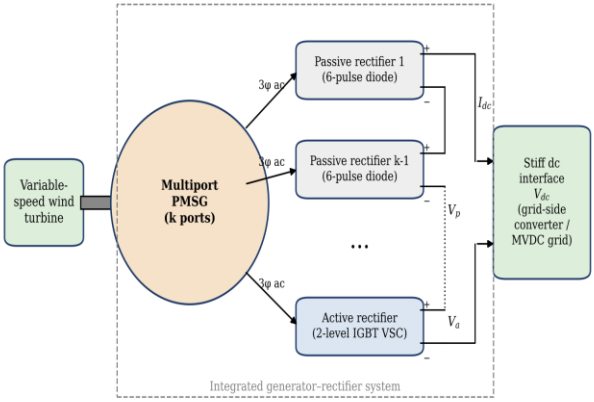


Figure 3.1: Integrated generator–rectifier wind energy conversion system (k-port PMSG, k−1 passive rectifiers and one active rectifier in series)

The subsystems are modelled in the following sections: turbine aerodynamics, drive train, generator ports, passive rectifiers, active rectifier and the dc-side power-flow relation.

3.2 WIND TURBINE AERODYNAMIC MODEL

The mechanical power extracted from the wind by a turbine of blade radius R is [29], [48]

$$P_m = \tfrac{1}{2} \rho \pi R^2 C_p(\lambda, \beta) v_w^3 \quad (3.1)$$

where ρ is the air density, v_w the wind speed, β the pitch angle and C_p the power coefficient. C_p depends on the tip-speed ratio

$$\lambda = \omega_m R / v_w \quad (3.2)$$

where ω_m is the rotor mechanical speed. In this work the widely used empirical model of Heier [48], [49] is adopted with β = 0 (pitch control is inactive below rated wind speed):

$$C_p(\lambda) = 0.5176\,(116/\lambda_i - 5)\,e^{-21/\lambda i} + 0.0068\,\lambda,$$
$$1/\lambda_i = 1/\lambda - 0.035 \qquad (3.3)$$

The resulting characteristic is shown in Fig. 3.2. The maximum $C_{p,max} = 0.480$ occurs at the optimum tip-speed ratio $\lambda_{opt} = 8.10$.

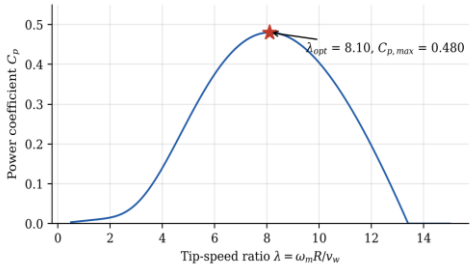


Figure 3.2: Power coefficient versus tip-speed ratio of the turbine model

The rotor diameter is 164 m (R = 82 m) and the air density 1.15 kg/m^3, as in the base paper [1]. With these values, (3.1) gives 10.07 MW at the rated wind speed of 12 m/s, which matches the 10 MW rating. Fig. 3.3 shows the mechanical power versus rotor speed for several wind speeds. Connecting the peaks gives the maximum-power curve

$$P^* = K_{opt}\,\omega_m^3,$$
$$K_{opt} = \tfrac{1}{2}\,\rho\,\pi\,R^5\,C_{p,max} / \lambda_{opt}^3 \qquad (3.4)$$

which, for the present turbine, gives $K_{opt} = 6.05 \times 10^6$ W·s^3/rad^3. The reference is limited to 10 MW above rated speed, so the rated rotor speed is $\omega_{m,rated} = 1.182$ rad/s.

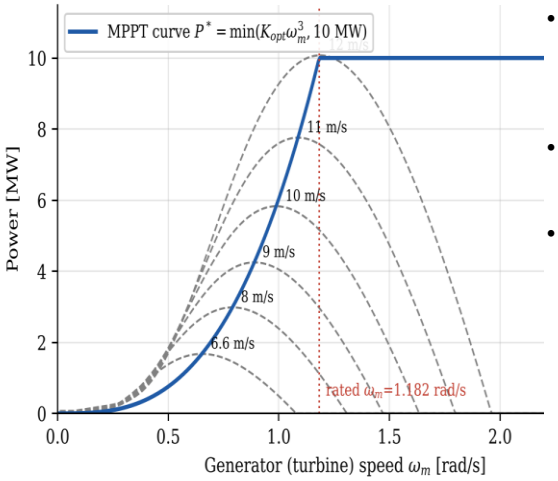


Figure 3.3: Mechanical power curves of the 10 MW turbine and the maximum-power (MPPT) curve

3.9 SYSTEM PARAMETERS

The parameters used throughout the thesis are listed in Table 3.1.

Table 3.1: System parameters used in simulation

Parameter	Symbol	Value
Rated power	P_{rated}	10 MW
Rotor diameter / blade radius	D / R	164 m / 82 m
Air density	ρ	1.15 kg/m^3
Optimum tip-speed ratio / $C_{p,max}$	λ_{opt} / $C_{p,max}$	8.10 / 0.480
Rated wind speed	v_{rated}	12 m/s
Rated rotor speed	$\omega_{m,rated}$	1.182 rad/s
Inertia (scaled, as in [1])	J	28.7 × 10^6 kg·m^2
Number of ac ports	k	3 (2 passive, 1 active)
Pole pairs	p	106
Rated frequency / peak EMF	f_0 / E_0	20 Hz / 1.1 kV
Port resistance / inductance	R / L	12 mΩ / 0.47 mH
Phase shift between passive ports	—	π/6 rad (electrical)
DC interface voltage	V_{dc}	5.7 kV
Active-rectifier dc capacitor	C_a	20 mF
Carrier frequency / control sampling	f_{sw} / T_c	2 kHz / 250 µs
Power-loop / MPPT sampling	T_p	1 ms
Integration step	Δt	50 µs

4.CONVENTIONAL CASCADED PI CONTROL (BASE PAPER)

4.1 CONTROL OBJECTIVES

The control system of the integrated generator–rectifier has three objectives [1]:

- to track the maximum power point of the turbine by forcing the dc-bus power to follow the MPPT reference;
- to regulate the active-rectifier d-axis current, which governs the power flow (3.13);
- to keep the q-axis current at zero so that the active rectifier operates at unity power factor.

Because the passive rectifiers are uncontrolled, all three objectives must be achieved through the voltage references of the single active rectifier. The base paper realises this with the cascaded architecture of Fig. 4.1: an MPPT block, an outer power PI regulator and inner dq

current PI regulators with feed-forward compensation.

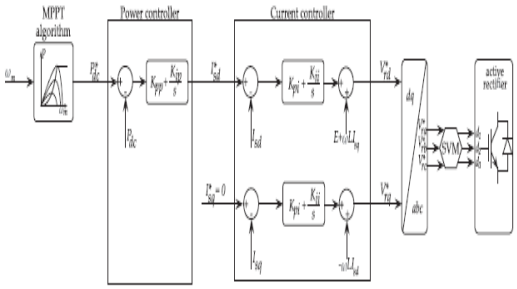


Figure 4.1: Cascaded PI control structure of the base paper applied to the active rectifier

4.2 MPPT ALGORITHM

The MPPT block implements the optimal-power-curve method [10], [24]. The measured rotor speed is mapped to the power reference $P^*_{dc} = \min(K_{opt}\omega_m^3, P_{rated})$ of (3.4). When the turbine runs below its optimal speed, the mechanical power exceeds the electrical power drawn, the rotor accelerates, and the reference rises; above the optimal speed the opposite occurs. The operating point therefore converges to the intersection of the MPPT curve with the mechanical power curve of the prevailing wind speed (Fig. 3.3). The method needs no anemometer, but its speed of convergence is set by the turbine inertia. The MPPT block is identical for the PI and ANN controllers so that the comparison isolates the effect of the power and current regulators.**Table 4.1:** Gains of the benchmark PI controllers

Gain	Symbol	Valu
Current-loop proportional gain	K_{pi}	0.295 V
Current-loop integral gain	K_{ii}	30.2 V/(
Current-loop bandwidth	α_c	$2\pi \times 100$
Power-loop proportional gain	K_{pp}	2.56×10
Power-loop integral gain	K_{ip}	1.29×10^{-2}
Power-loop design crossover	ω_p	$2\pi \times 8$ r
d-axis current limit	$I_{sd,max}$	3.3 k

4.5 FREQUENCY-RESPONSE VERIFICATION

The open-loop frequency responses of both loops, including the 1.5-sample modulation and computation delay of the current loop and the dc-side and sampling lags of the power loop, are shown in Fig. 4.2. The current loop crosses over at 100 Hz with a phase margin of 70°, and the power loop crosses over at 8.1 Hz with a phase margin of 81°. Both loops are therefore well damped at the rated operating point, and the frequency separation of more than one decade justifies the cascaded design.

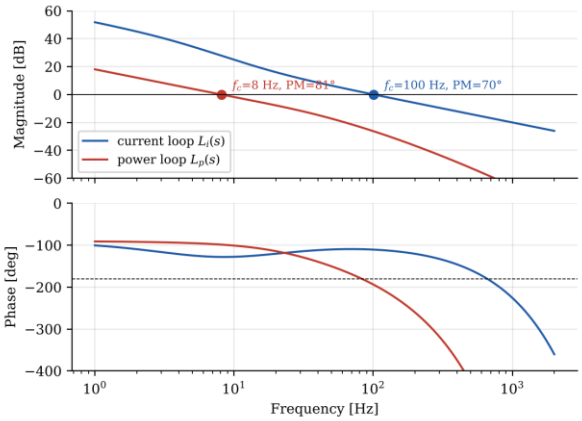


Figure 4.2: Open-loop frequency responses of the PI current loop and power loop at rated operating point

5.PROPOSED ANN-BASED CONTROLLER

5.1 FUNDAMENTALS OF ARTIFICIAL NEURAL NETWORKS

An artificial neural network is a parallel structure of simple processing units (neurons) connected by weighted links [43]. Each neuron (Fig. 5.1) forms a weighted sum of its inputs plus a bias and passes it through an activation function:

$$y = \varphi(\Sigma_i w_i x_i + b) \quad (5.1)$$

In a multilayer perceptron (MLP), neurons are arranged in an input layer, one or more hidden layers and an output layer. With a nonlinear activation such as the hyperbolic tangent in the hidden layers and linear output neurons, an MLP can approximate any continuous function on a compact set to arbitrary accuracy [36]. This property makes MLPs suitable for representing

the nonlinear inverse of the power-flow relation (3.13) and the inverse dq dynamics of the active rectifier.

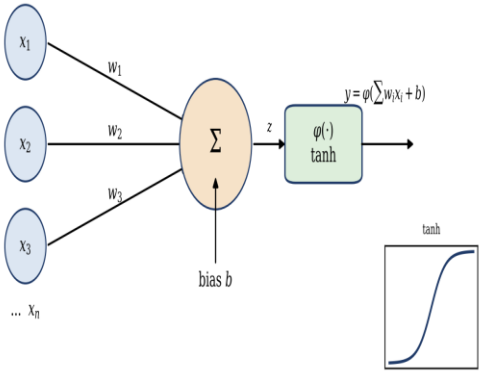


Figure 5.1: Model of an artificial neuron with tanh activation

5.2 RATIONALE FOR THE PROPOSED ANN CONTROLLER

Several ANN control structures are possible: an ANN trained to imitate an existing PI controller, a direct inverse controller, an indirect (model-based) controller or a reinforcement-learning controller [39], [38]. Imitating the PI would inherit its bandwidth limits. The present design instead exploits the fact that the plant equations (3.8), (3.9) and (3.13) are known well enough to generate training data, while their parameters are uncertain. The proposed controller therefore combines:

- **offline-trained inverse models** that compute, in one step, the control input needed to produce the desired output over the whole operating envelope; and
- **on-line Lyapunov-based adaptation** of the output layer, driven by the error between the plant and a reference model, which corrects for parameter mismatch and removes steady-state error [40], [41].

This neuro-adaptive structure replaces both PI regulators of the cascade. The MPPT block is unchanged.

5.3 OVERALL STRUCTURE OF THE ANN CONTROL SYSTEM

The proposed control system is shown in Fig. 5.2. The power-loop ANN (ANN-P) receives the MPPT power reference, the electrical speed and the measured dc-bus voltage and outputs the d-axis current reference. The current-loop ANN (ANN-C) receives the dq current references and measurements and the electrical speed, and outputs both dq voltage references. Both networks have adaptive output layers. The voltage references pass through the usual dq→abc transformation and space-vector modulation.

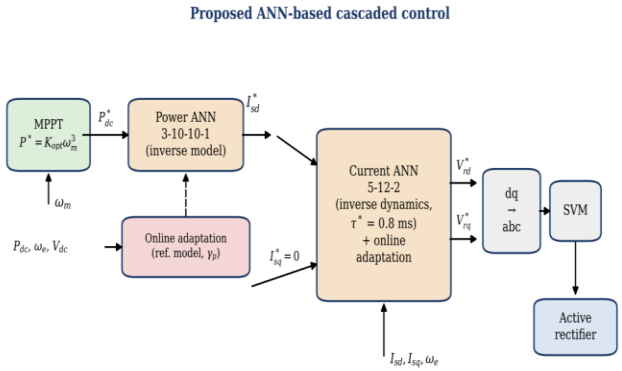


Figure 5.2: Proposed ANN-based cascaded control of the active rectifier

The design procedure followed for both networks is summarised in Fig. 5.3.

6.SIMULATION RESULTS AND COMPARATIVE ANALYSIS

6.1 SIMULATION PLATFORM AND SCENARIOS

The system model of Chapter 3 and both controllers were implemented as a discrete-time average-value simulation in Python (NumPy/SciPy) with a fixed integration step of 50 µs. The controllers run at their own sampling rates: the current loop at 4 kHz with a one-sample computation delay, and the power/MPPT loop at 1 kHz. The structure of the

simulation is shown in Fig. 6.1. Each block corresponds one-to-one to a MATLAB/Simulink average-value implementation, so the model can be transferred directly to that environment. Switching-ripple effects of the active rectifier and the six-pulse ripple of the diode bridges are not represented, because the passive-rectifier ripple is already minimised by phase shifting (Section 3.5) and the study concentrates on controller dynamics.

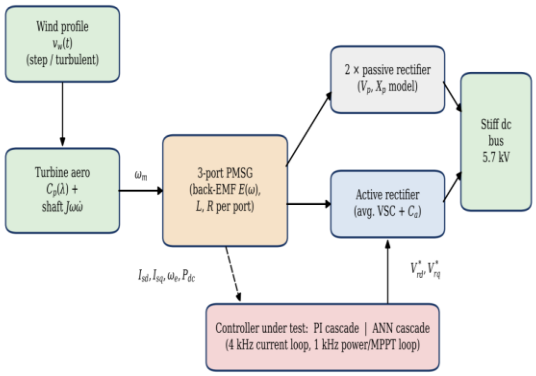


Figure 6.1: Structure of the simulation model used for PI and ANN evaluation

The two controllers were compared over the six scenarios of Table 6.1. Identical plant models, MPPT blocks, limits and sampling rates were used for both, so that differences in the results are due only to the power and current regulators.

Table 6.1: Simulation scenarios

No.	Scenario	Description
S1	Power steps, rated speed	Speed fixed at 1.182 rad/s; P^*_{dc}: 2 → 6 → 10 → 4 MW at 0.3, 0.8, 1.3 s
S2	Power steps, low speed	Speed fixed at 70 % of rated; P^*_{dc}: 1 → 2.5 → 3.4 → 1.5 MW
S3	Parameter mismatch	As S1 (peak 9 MW) with E_0 −8 %, L +40 %, R +50 % in the plant, controllers unchanged
S4	DC-bus voltage sag	P^*_{dc} = 8 MW; V_{dc} ramps 5.7 → 5.415 kV (−5 %) in 20 ms at 0.3 s and recovers at 0.8 s
S5	MPPT, step wind	Turbine starts at 55 % rated speed; wind 12 → 10 → 11 m/s at 5.5 s and 10.5 s (base-paper case)
S6	MPPT, turbulent wind	40 s of turbulent wind (mean 10 m/s, 12 % turbulence intensity plus slow gust)

Performance is quantified by the 10–90 % rise time t_r, the percentage overshoot M_p, the 2 % settling time t_s, the steady-state error e_{ss}, the integral of absolute error IAE = $\int|P^*_{dc} - P_{dc}|dt$ and the integral of time-weighted absolute error ITAE = $\int t|P^*_{dc} - P_{dc}|dt$. For MPPT, the energy delivered to the dc bus, the ratio to the maximum available energy and the RMS power-tracking error are used.

6.2 VALIDATION OF THE SIMULATION MODEL

Before comparing controllers, the model was checked against the analytical relation (3.13). For each of the three electrical speeds 38π, 40π and 42π rad/s used in the base paper, eight power references were applied and the steady-state values of I_{sd} and P_{dc} were recorded with both controllers. Fig. 6.2 shows that all simulated points lie on the analytical curves; the largest deviation is below 0.002 %. This confirms that the dynamic model is consistent with the base-paper analysis and that both controllers drive the system to the same steady states.

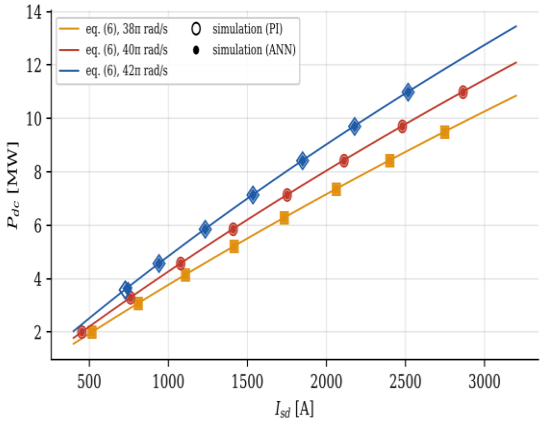


Figure 6.2: Validation of the simulation model: steady-state points (markers) against (3.13) (lines)

6.3 SCENARIO S1: POWER-REFERENCE STEPS AT RATED SPEED

Fig. 6.3 shows the dc-bus power for the sequence of reference steps at rated speed, and Fig. 6.4 expands each step. The PI controller

follows the reference smoothly without overshoot but slowly, with rise times of 38–43 ms and settling times of 73–82 ms. The ANN controller reaches the new power level within 5–7 ms and settles within 10–26 ms, because ANN-P computes the required current directly from the learned inverse model instead of accumulating it through an integrator.

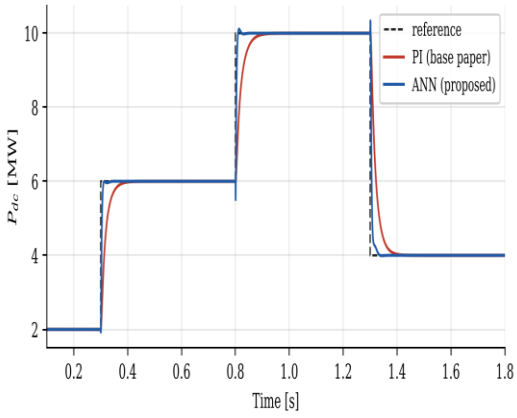


Figure 6.3: Scenario S1: dc-bus power response to reference steps at rated speed

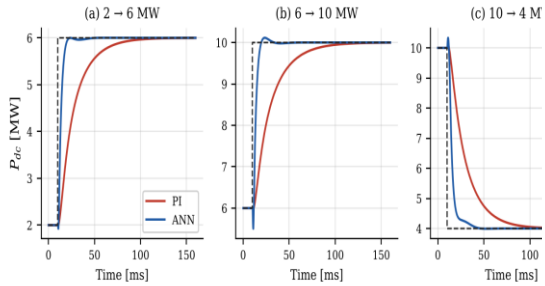


Figure 6.4: Scenario S1: expanded view of the three power steps

The zoomed traces reveal a feature that deserves attention: immediately after a large upward step, the ANN response first dips (to 5.5 MW for the 6 → 10 MW step) before rising, and after the downward step it briefly rises to 10.3 MW. This is a non-minimum-phase effect of the integrated topology. A fast increase of I_{sd} requires a sharp reduction of V_{rd} to drive current into the port inductance, which momentarily reduces the active-rectifier power P_a, discharges C_a and lowers V_a and hence I_{dc} (3.12). The slower PI controller excites this effect much less (minimum 5.98 MW). The transient lasts about 3 ms and does not affect the settling behaviour, but it should be considered when the controller is applied to a real converter, for example by rate-limiting large reference changes.

The d- and q-axis currents are shown in Fig. 6.5. Both controllers track the current references, but ANN-C tracks with a much smaller error (steady RMS d-axis tracking error below 0.001 A, compared with 0.03–0.05 A for the PI). The q-axis current, which should remain at zero, shows short spikes at each step. These are larger with the ANN (peaks of 32–59 A) than with the PI (4–6 A) because the faster d-axis response excites the cross-coupling more strongly; they decay within a few milliseconds and remain below 2.5 % of the rated d-axis current. Fig. 6.6 shows that the active and passive rectifier voltages move in opposite directions as the power changes, while their sum remains equal to the constant 5.7 kV bus.

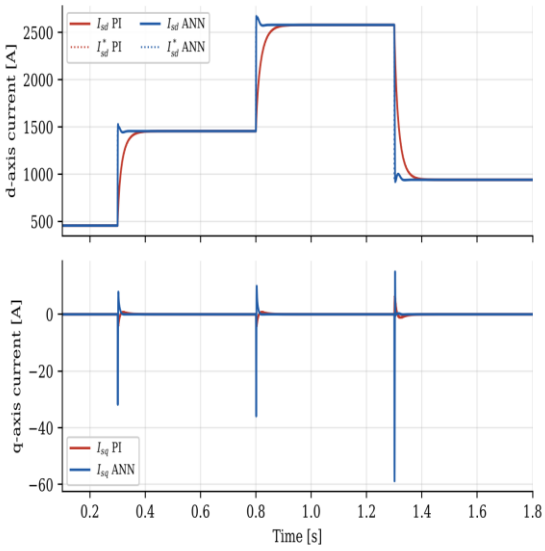


Figure 6.5: Scenario S1: active-rectifier d-axis and q-axis currents

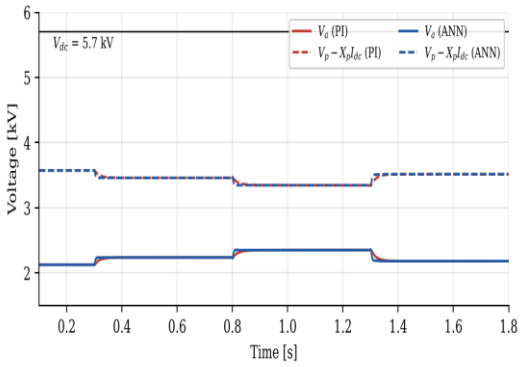


Figure 6.6: Scenario S1: active-rectifier voltage V_a and passive-rectifier output voltage The quantitative results are given in Table 6.2.

Step	Controller	t_r [ms]	M_p [%]	t_s [ms]	e_{ss} [%]	IAE [MW·s]	ITAE [MW·s^2]
1→2.5 MW	PI	83.3	0	151.3	0	0.0583	22.3×10^{-4}
1→2.5 MW	ANN	5	0	10.3	0	0.0059	0.3×10^{-4}
2.5→3.4 MW	PI	85.3	0	155.3	0	0.0363	14.2×10^{-4}
2.5→3.4 MW	ANN	4.7	0.77	9	0	0.0036	0.1×10^{-4}
3.4→1.5 MW	PI	82.8	0	150.5	0.001	0.0754	28.6×10^{-4}
3.4→1.5 MW	ANN	4.8	0.03	9.2	0	0.0075	0.2×10^{-4}

Table 6.2: Scenario S1 — power-step performance at rated speed

6.4 SCENARIO S2: POWER STEPS AT LOW GENERATOR SPEED

At 70 % speed the slope of (3.13) is lower than at the rated point, so the loop gain of the fixed-gain power PI falls. Fig. 6.7 and Table 6.3 show that the PI rise time doubles to about 83–85 ms and the settling time increases to 150–155 ms. The ANN controller is essentially unaffected, because the speed is an input to ANN-P and the learned inverse automatically supplies the correct current: rise times remain at 4.7–5.0 ms and settling times at 9–10 ms. The IAE of the ANN is about one tenth of that of the PI. This scenario demonstrates the main structural advantage of the ANN: operating-point-independent dynamics.

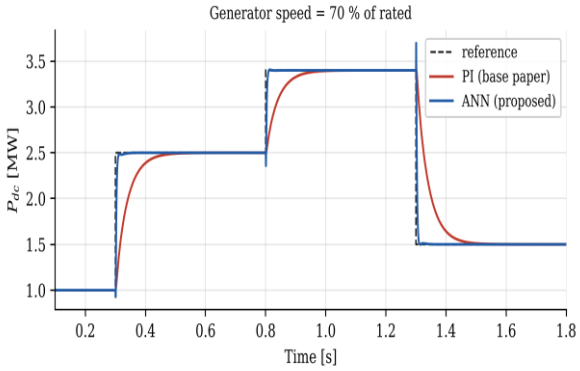


Figure 6.7: Scenario S2: dc-bus power response at 70 % of rated speed

Table 6.3: Scenario S2 — power-step performance at 70 % of rated speed

Step	Controller	t_r [ms]	M_p [%]	t_s [ms]	e_{ss} [%]	IAE [MW·s]	ITAE [MW·s^2]
1→2.5 MW	PI	83.3	0	151.3	0	0.0583	22.3×10^{-4}
1→2.5 MW	ANN	5	0	10.3	0	0.0059	0.3×10^{-4}
2.5→3.4 MW	PI	85.3	0	155.3	0	0.0363	14.2×10^{-4}
2.5→3.4 MW	ANN	4.7	0.77	9	0	0.0036	0.1×10^{-4}
3.4→1.5 MW	PI	82.8	0	150.5	0.001	0.0754	28.6×10^{-4}
3.4→1.5 MW	ANN	4.8	0.03	9.2	0	0.0075	0.2×10^{-4}

Scenario	Controller	Energy to dc bus [kWh]	Max. available [kWh]	Capture ratio [%]	RMS power-tracking error [kW]
S5 step wind	PI	27.239	33.077	82.35	14
S5 step wind	ANN	27.224	33.077	82.31	4.9
S5′ step wind + mismatch	PI	26.643	33.077	80.55	19.8
S5′ step wind + mismatch	ANN	26.629	33.077	80.51	10.5
S6 turbulent wind	PI	41.907	45.882	91.34	8.5
S6 turbulent wind	ANN	41.898	45.882	91.32	2.6

Table 6.6: Scenarios S5 and S6 — MPPT energy capture and tracking accuracy

6.9 COMPARATIVE ANALYSIS OF PI AND ANN CONTROLLERS

The rise and settling times of all step tests are compared in Fig. 6.18, and the IAE values in Fig. 6.19. The ANN gives the shortest rise and settling times and the lowest IAE in every case.

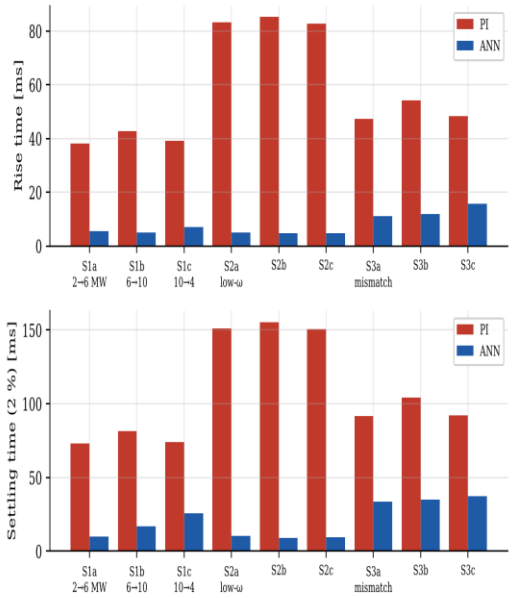


Figure 6.18: Comparison of rise time and settling time for PI and ANN in scenarios S1–S3

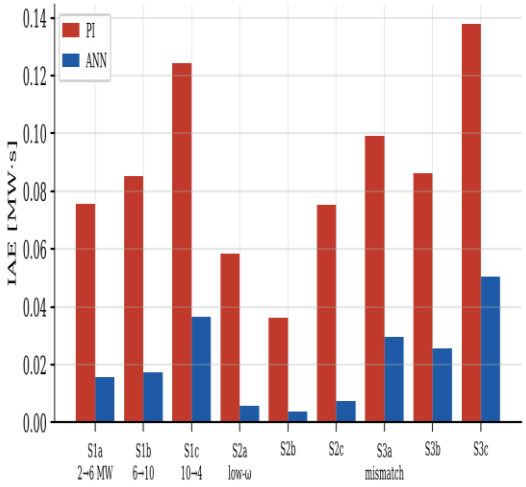


Figure 6.19: Comparison of IAE for PI and ANN in scenarios S1–S3

The overall comparison is given in Table 6.7. Averaged over the three steps of each scenario, the ANN reduces the rise time by 85 % at rated speed, 94 % at low speed and 74 % with parameter mismatch; the settling time by 77 %, 94 % and 63 %; and the IAE by 76 %, 90 % and 67 %, respectively.

Table 6.7: Overall comparison of PI and ANN controllers

Performance index	PI (base paper)	ANN (proposed)	Improvement
Mean rise time, S1 [ms]	40	5.8	85 % faster
Mean settling time, S1 [ms]	76.3	17.6	77 % faster
Mean IAE, S1 [MW·s]	0.095	0.023	76 % lower
Maximum overshoot, S1 [%]	0	2.9	PI better
Mean rise time, S2 low speed [ms]	83.8	4.8	94 % faster
Mean settling time, S2 [ms]	152.4	9.5	94 % faster
Mean rise time, S3 mismatch [ms]	50	12.9	74 % faster
Mean settling time, S3 [ms]	96	35.3	63 % faster
Mean IAE, S3 [MW·s]	0.108	0.035	67 % lower
Recovery after V_{dc} sag, S4 [ms]	59.1	40.8	31 % faster
Peak q-axis current in S1 [A]	6.4	58.8	PI better
Steady-state error (all cases)	≈ 0	≈ 0	equal
RMS MPPT tracking error, S5 [kW]	14	4.9	65 % lower
RMS MPPT tracking error, S6 [kW]	8.5	2.6	69 % lower
MPPT energy capture, S5 / S6 [%]	82.35 / 91.34	82.31 / 91.32	equal (< 0.06 %)
Dependence on operating point	strong	negligible	ANN better
Use of plant knowledge	none	learned inverse model	ANN better
Design / tuning effort	low	moderate (data, training)	PI better
Computational load	very low	low (≈ 260 MAC/cycle)	PI better

7.1 CONCLUSION

This thesis extended the integrated generator–rectifier wind energy system of Huynh, Tungare and Banerjee [1] by replacing the cascaded PI power and current regulators of the active rectifier with an ANN-based neuro-adaptive controller, and evaluated the extension entirely through simulation. The main conclusions are:

- An average-value model of the 10 MW system with a three-port PMSG, two phase-shifted passive rectifiers and one active rectifier was developed. Its steady state agrees with the analytical power-flow relation of the base paper to better than 0.002 %, confirming that the d-axis current of a single active rectifier controls the total power of the system.
- The PI benchmark, tuned by internal model control with 100 Hz current-loop and 8 Hz power-loop crossover frequencies, provides stable, overshoot-free power tracking with rise times of about 40 ms at rated speed, increasing

to about 84 ms at 70 % speed because of the speed-dependent plant gain.

- Two compact MLPs (3-10-10-1 for the power loop and 5-12-2 for the current loop) trained with the Levenberg–Marquardt algorithm reproduce the inverse power-flow relation and the inverse dq dynamics with test correlation coefficients above 0.9999997 and errors below 0.15 % of range.
- With reference-model-based on-line adaptation of the output layers, the ANN controller reduces the mean rise time by 85 %, the settling time by 77 % and the IAE by 76 % at rated speed. At low speed the reductions grow to about 94 %, 94 % and 90 %, showing that the ANN removes the operating-point dependence of the PI.
- Under an 8 % reduction of the EMF constant, a 40 % increase of inductance and a 50 % increase of resistance, both controllers retain zero steady-state error, and the ANN still settles about 2.7 times faster than the PI with 63–70 % lower IAE.
- During MPPT, the ANN reduces the RMS power-tracking error by 65–69 % under both step and turbulent wind. However, the energy delivered to the dc bus is the same for both controllers to within 0.06 %, because energy capture is governed by the slow rotor dynamics.
- The ANN produces a brief non-minimum-phase dip of the dc-bus power after large upward steps and larger transient q-axis currents (up to about 2.3 % of rated current), which are the costs of its faster response.

Overall, the proposed ANN controller makes the power-flow control of the integrated generator–rectifier system substantially faster, more accurate and less dependent on the operating point, while keeping the MPPT energy yield unchanged. These properties are valuable for offshore wind turbines connected to dc collection grids, where fast and well-damped power control supports grid stability and reduces drive-train stress.

7.2 FUTURE SCOPE

The work can be extended in several directions:

- **Switched-model and Simulink validation.** The controllers should be evaluated with a detailed switching model of the active rectifier and diode bridges in MATLAB/Simulink or PLECS, including ripple, dead time and measurement noise.
- **Hardware-in-the-loop and experimental verification.** Implementing ANN-P and ANN-C on a DSP or FPGA and testing them on a scaled multiport-generator prototype, similar to that of [1], would confirm the real-time feasibility.
- **Mitigation of the non-minimum-phase transient.** Rate limiting of the d-axis reference, a feed-forward of the dc-link capacitor energy, or model predictive control could reduce the power dip after large steps.
- **Learning-based MPPT layer.** Since energy capture is limited by the MPPT layer, combining the ANN power loop with an intelligent MPPT algorithm or wind-speed estimator [50]–[52] could improve energy yield under turbulent wind.
- **Reinforcement-learning control.** Training the controller directly on the closed-loop cost with adaptive dynamic programming [38] could jointly optimise speed of response and q-axis coupling.
- **Fault ride-through and grid interaction.** The behaviour of the ANN-controlled system during dc-grid faults, generator port faults and passive-rectifier failures should be investigated.
- **Above-rated operation.** Coordination with pitch control above rated wind speed and with active ripple compensation [21] remains to be studied.

REFERENCES

[1] P. Huynh, S. Tungare, and A. Banerjee, "Maximum power point tracking for wind turbine using integrated generator–rectifier systems," IEEE Trans. Power Electron., vol. 36, no. 1, pp. 504–512, Jan. 2021.

[2] D. S. Ottensen, "Global offshore wind market report," Norwegian Energy Partners, Oslo, Norway, Tech. Rep., 2018.

[3] C. Bak et al., "Light rotor: The 10-MW reference wind turbine," in Proc. Eur. Wind Energy Conf. Exhib., 2012, pp. 1–10.

[4] P. Higgins and A. Foley, "The evolution of offshore wind power in the United Kingdom," Renew. Sustain. Energy Rev., vol. 37, pp. 599–612, 2014.

[5] W. Musial, P. Beiter, P. Spitsen, J. Nunemaker, and V. Gevorgian, "2018 offshore wind technologies market report," National Renewable Energy Laboratory, Golden, CO, USA, Tech. Rep., Aug. 2019.

[6] Siemens Gamesa, "SG 10.0-193 DD offshore wind turbine," product information, 2019.

[7] GE Renewable Energy, "Haliade-X 12 MW offshore wind turbine platform," product information, 2019.

[8] MHI Vestas Offshore Wind, "The world's most powerful available wind turbine gets major power boost," press release, Dec. 2017.

[9] V. Yaramasu, B. Wu, P. C. Sen, S. Kouro, and M. Narimani, "High-power wind energy conversion systems: State-of-the-art and emerging technologies," Proc. IEEE, vol. 103, no. 5, pp. 740–788, May 2015.

[10] M. Chinchilla, S. Arnaltes, and J. C. Burgos, "Control of permanent-magnet generators applied to variable-speed wind-energy systems connected to the grid," IEEE Trans. Energy Convers., vol. 21, no. 1, pp. 130–135, Mar. 2006.